Progress In Electromagnetics Research C, Vol. 123, 101–116, 2022

Analysis on the Spatial Impedance of the Wireless Power Transfer System in the Near Field

Jianwei Kang*, Jie Lu, Deyu Zeng, and Xiangyang Shi

Abstract—In this paper, the spatial impedance of the wireless power transfer (WPT) system is analyzed, and a resistance tunnel is found. First, the definitions of the spatial impedance in the near field are discussed, and one definition is chosen. By using this definition, the concept of the resistance and the reactance are extended from a scaler form into a vector form. Under this definition and this concept, the spatial impedance is analyzed, and a resistance tunnel is found. The tunnel possesses an obvious direction which is from the receive coil to the transmit coil, and possesses a concave phenomenon on the resistance's magnitude curves. The reason for the forming of the tunnel is also analyzed by discussing the x- and z-components of the resistance. Second, the influences on the resistance tunnel by four factors are discussed. Only the current phase difference determines the existence of the resistance tunnel. The other factors only influence the magnitude and distribution of the resistance. The correctness of the theoretical calculation is verified by implementing an electromagnetic simulation via FEM. Since the WPT system is one of the typical coupling systems in the near field, one can infer that the resistance tunnel not only exists in the WPT system, but also exists in other coupling coil systems in the near field.

1. INTRODUCTION

Wireless power transfer (WPT) is a power transmitting technology [1–3]. One of the popular research fields in WPT area is the electromagnetic field analysis. One area is the theoretical analysis of the electromagnetic field in WPT, which includes the modeling and the calculation of the electromagnetic field in WPT [4–6], and the analysis on the characteristic of electromagnetic field [7, 8]. Another area is aiming at the practical application based on the electromagnetic field. Those researches include foreign object detection [9], electromagnetic compatibility (EMC) and human exposure assessment [10, 11], the design of coils and shields [12, 13], etc.

Many achievements have been obtained from those researches, but the analysis on the spatial impedance distribution of the WPT system in the near field is less researched. The research in [14] studied the modeling of multi-layers and obtained a lumped impedance model. The research in [15] modeled the spatial impedance by S-parameter. The concept of the lumped impedance and S-parameter of the WPT system in the literature is not the concept of the spatial distributed impedance. The impedance distribution is spatially distributed, which means that every point in the space of energy transferred region in the WPT system possesses one impedance value.

On the other hand, the related researches on impedance are also a traditional research spot [16–19], not only in WPT areas. Spatial impedance is also a concentration by researchers in both theoretical analysis and practical application. The researches from a theoretical view include the modeling of surface impedance [20, 21], the analysis on the electromagnetic field distribution by surface impedance [22], the

Received 26 May 2022, Accepted 4 August 2022, Scheduled 26 August 2022

* Corresponding author: Jianwei Kang (kjw689@163.com).

The authors are with the Key Laboratory of Testing Technology for Manufacturing Process, Ministry of Education, School of Manufacturing Science and Engineering, Southwest University of Science and Technology, Mianyang 621010, China.

analysis on impedance boundary [23], the modeling of a transmission line via distributed impedance [24], etc. Moreover, most researches have mentioned and used spatial impedance for a practical application. A development of an optics cloak shell via electromagnetic impedance is presented in [25], and it shows an idea to analyze different directions of impedance on one point, which means that the impedance in space is a vector but not a scaler. The researches in [26] gave a definition of the spatial impedance. The study in [27] illustrated that the wave impedance can imply the mechanism and the region of the energy transferring.

Although those researches are worth to be used for reference in the further research, the analyzed spatial impedance of those researches is in the far field, and the results cannot be directly used in this paper in which the near field situation will be considered. In the far field of free space, the spatial impedance is a constant $377\,\Omega$. If one obtains the electric field, one can deduce the magnetic field by the spatial impedance. However, in the near field, the spatial impedance is more complex and has been less researched. One of the researches calculates the near field spatial impedance and uses the value of the spatial impedance to classify the near field and far field in [28], which shows that the analysis on the spatial impedance has a physical value. The research [29] shows that the magnitude of the spatial impedance in the near field is smaller than that in the far field. In [30], there is a definition of spatial impedance. However, it is worth noting that although there are many analyses on the spatial impedance in the near field, the definition of the spatial impedance in the near field is not unified.

Based on those researches, more problems of the spatial impedance in the near field can be analyzed. Those problems include what the spatial impedance distribution is, what characteristic of the spatial impedance possesses, and what relation is between the spatial impedance and the transferred power in a WPT system, because the WPT system is a typical coil coupling system in the near field.

This paper analyzes the spatial impedance of a WPT system in the near field and finds that a resistance tunnel exists. The resistance tunnel possesses a direction which is from the receiving coil to the transmitting coil. The main value of the resistance tunnel region is about $0.5\,\Omega$ under the typical working condition. This discovery illustrates the mechanism of the energy transferred from a spatial impedance view. Then, the probable influence factors of the resistance tunnel are also discussed. The results show that only the current phase difference between the transmitting and receiving coils determines the existence of the resistance tunnel. Finally, the theoretical analysis is proved by using an electromagnetic simulation by FEM. The discovery of the resistance tunnel in the WPT system gives a deep understanding of how energy transfers from coils to coils from the spatial impedance view. On the other hand, the research on the impedance characteristic of a WPT system can gives valuable reference in other analyses on the coils coupling system in the near field.

The arrangement of this paper is as follows. In Section 2, we deduce the spatial impedance by using the direct calculation method of Biot-Savart law. In Section 3, a WPT experimental system on the typical working condition is constructed and analyzed, and the spatial impedance distributions are presented. The spatial impedance is in the form of vector and in the form of the complex, hence an arrow map and a magnitude distribution of the resistance and reactance are depicted. In Section 4, four factors are discussed, which are the operating frequency in the WPT system, current magnitude ratio, current phase difference, and different coil types. The influences of those four factors on spatial impedance are discussed. In Section 5, the theoretic analysis is proofed by using the ANSYS Electromagnetic Suits. The last Section 6 draws a conclusion.

2. FORMULA DEDUCING

2.1. The Magnetic Field Intensity and Its Components

Figure 1 shows a simplified WPT system of two coils. Considering axial symmetry, only the xoz plane is taken into account. Based on this system, the spatial impedance at the arbitrary point will be deduced. Coil 1 and coil 2 represent the transmitting coil and receiving coil, respectively. Both coil 1 and coil 2 possess a radius R equal to 0.1 m. The currents carried by coil 1 and coil 2 are

$$i_1(t) = I_m \cos(\omega t) \tag{1}$$

$$i_2(t) = kI_m \cos(\omega t + \Delta\phi) \tag{2}$$

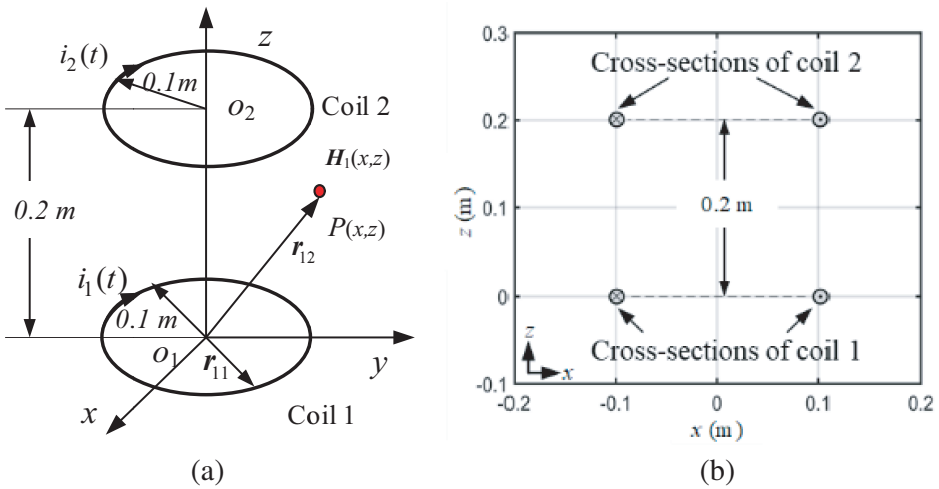

Figure 1. WPT system of two coils.

where ω is the angular frequency, I_m the magnitude of the current, k the currents magnitude ratio, and $\Delta\phi$ the current phase difference. Subscripts 1 and 2 refer to coil 1 and coil 2, respectively. For simplification, the currents and other variables containing t parameter in the following sections are transformed in the format of phasors. Hence, currents 1 and 2 can be expressed as

$$\dot{I}_1 = I_m \tag{3}$$

$$\dot{I}_2 = kI_m\angle\Delta\phi \tag{4}$$

Those two currents will generate electromagnetic fields in the transmitting area of the WPT system. The magnetic field intensity generated by coil 1 is $\dot{H}_1(x,z)$. According to the Biot-Savart law, the magnetic field generated by coil 1 can be expressed as

$$\dot{H}_1(x,z) = \oint_{l_1} \frac{I_m \mathrm{d}l_1 \times (r_{12} - r_{11})}{4\pi \left|r_{12} - r_{11}\right|^3} \tag{5}$$

where r_{12} is the field point vector, and r_{11} is the source point vector. $\mathrm{d}l_1$ is the integral unit.

$\dot{H}_1(x,z)$ is combined by the x-component $\dot{H}_{1x}(x,z)$ and z-component $\dot{H}_{1z}(x,z)$. The relationship of the three quantities is

$$H_1(x,z)=H_{1x}(x,z)e_x+H_{1z}(x,z)e_z = \dot{I}_1T_{1x}(x,z)e_x + \dot{I}_1T_{1z}(x,z)e_z \tag{6}$$

where e_x and e_z are the unit x and z direction vectors. $T_{1x}(x,z)$ and $T_{1z}(x,z)$ are the geometrical functions, which are defined as:

$$T_{1x}(x,z) = \frac{1}{4\pi}\int_0^{2\pi} \frac{\cos\Phi_1 \cdot R(z-z_1)d\Phi_1}{\left[x^2+R^2-2xR\cos\Phi_1+(z-z_1)^2\right]^{3/2}} \tag{7}$$

$$T_{1z}(x,z) = \frac{1}{4\pi}\int_0^{2\pi} \frac{(R^2-\cos\Phi_1 Rx)d\Phi_1}{\left[x^2+R^2-2xR\cos\Phi_1+(z-z_1)^2\right]^{3/2}} \tag{8}$$

Equations (7) and (8) rather than (5) are used to calculate the magnetic field. The method is introduced in [31] and is called as direct calculation method.

Similarly, the magnetic field generated by coil 2 can be expressed as:

$$H_2(x,z)=H_{2x}(x,z)e_x+H_{2z}(x,z)e_z = \dot{I}_2T_{2x}(x,z)e_x + \dot{I}_2T_{2z}(x,z)e_z \tag{9}$$

where $T_{2x}(x,z)$ and $T_{2z}(x,z)$ are the geometrical functions of coil 2 and can be expressed as:

$$T_{2x}(x,z) = \frac{1}{4\pi}\int_0^{2\pi} \frac{2}{\left[x^2+R^2-2xR\cos\Phi_2+(z-z_2)^2\right]^{3/2}} \tag{10}$$

$$T_{2z}(x,z) = \frac{1}{4\pi}\int_0^{2\pi} \frac{(R^2-\cos\Phi_2 Rx)d\Phi_2}{\left[x^2+R^2-2xR\cos\Phi_2+(z-z_2)^2\right]^{3/2}} \tag{11}$$

The total composed magnetic field is as follows

$$\dot{H}(x,z) = \dot{H}_1(x,z) + \dot{H}_2(x,z) = \dot{H}_x(x,z)e_x + \dot{H}_z(x,z)e_z \tag{12}$$

where

$$\dot{H}_x(x,z) = \dot{H}_{1x}(x,z)+\dot{H}_{2x}(x,z) = \dot{I}_1 T_{1x}(x,z) + \dot{I}_2 T_{2x}(x,z) \tag{13}$$

$$\dot{H}_z(x,z) = \dot{H}_{1z}(x,z)+\dot{H}_{2z}(x,z) = \dot{I}_1 T_{1z}(x,z) + \dot{I}_2 T_{2z}(x,z) \tag{14}$$

Equations (12), (13), and (14) mean that the total superposed magnetic field is composed of two magnetic fields generated by two coils. The total composed magnetic field $\dot{H}(x,z)$ can also be divided into the x and z components, because the total magnetic field is a vector of the space and also is a phasor of the time. Each $\dot{H}_x(x,z)$ or $\dot{H}_z(x,z)$ component is also composed of two parts which are generated by two coils, respectively.

2.2. The Inductance Electric Field Intensity

In the WPT transfer space, the electric field is another important field. The whole electric field contains conservative field and solenoid field [32]. The conservative electric field is generated by a charge density, and the conservative electric field is usually neglected due to its relatively low value and weak influence [33]. The solenoidal electric field is due to the time-varying current, so it can be called the induced electric field. Therefore, only the solenoidal electric field will be taken into consideration in this paper, and the electric field generated by coil 1 can be expressed as:

$$\dot{E}_1(x,z) = -j\omega\dot{A}_1(x,z) \tag{15}$$

where $\dot{A}(x,z)$ is the magnetic vector potential, and it can also be calculated by using a geometrical function. Hence the electric field is

$$\dot{E}_1(x,z) = -j\mu_0\omega\dot{I}_1 T_{\mathrm{E1}}(x,z)e_y \tag{16}$$

where μ_0 is the magnetic permeability of free space. Notice that the electric field on the xoz plane only possesses the y-direction. $T_{\mathrm{E1}}(x,z)$ is the geometrical function of electric field generated by coil 1, and it can be expressed as:

$$T_{\mathrm{E1}}(x,z) = \frac{1}{4\pi}\int_0^{2\pi} \frac{\cos\Phi_1 R d\Phi_1}{(x^2+R^2-2xR\cos\Phi_1+(z-z_1)^2)^{1/2}} \tag{17}$$

Similarly, the electric field generated by coil 2 can be calculated as follows:

$$\dot{E}_2(x,z) = -j\mu_0\omega\dot{I}_2 T_{\mathrm{E2}}(x,z)e_y \tag{18}$$

$$T_{\mathrm{E2}}(x,z) = \frac{1}{4\pi}\int_0^{2\pi} \frac{\cos\Phi_2 R d\Phi_2}{(x^2+R^2-2xR\cos\Phi_2+(z-z_2)^2)^{1/2}} \tag{19}$$

Therefore, similar to the total magnetic field and its components, the total electric field can be expressed as:

$$\dot{E}(x,z) = \dot{E}_1(x,z) + \dot{E}_2(x,z) = -\mathrm{j}\omega\mu_0\left[\dot{I}_1 T_{\mathrm{E1}}(x,z) + \dot{I}_2 T_{\mathrm{E2}}(x,z)\right]e_y \tag{20}$$

2.3. The Spatial Impedance

Up to now, the electric and magnetic fields have been analyzed. Then the spatial impedance can be calculated as follows:

$$Z(x,z) = Z_x(x,z)e_x + Z_z(x,z)e_z \tag{21}$$

It is worth noting that there is no unified definition of spatial impedance in the near field. Hence there is a problem of how to define a spatial impedance, that is how to calculate $Z_x(x,z)$ and $Z_z(x,z)$. We know that the impedance is the ratio of electric field and magnetic field. But there are at least two components of magnetic field and one component of electric field on the xoz plane. The ratios can be in many forms, so the problem that to choose what ratio form is should be considered.

According to the results shown in the following sections, we define the spatial impedance in the near field as follows:

$$Z_x(x,z) = \frac{\dot{E}_y(x,z)}{\dot{H}_z(x,z)} \tag{22}$$

$$Z_z(x,z) = \frac{\dot{E}_y(x,z)}{\dot{H}_x(x,z)} \tag{23}$$

By using this definition, the spatial impedance has an obvious physical meaning in both directions and magnitude distributions, and a resistance tunnel will appear.

Then one brings Equations (14) and (20) into Equation (22), and we can obtain

$$Z_x(x,z) = \frac{\mathrm{j}\omega\mu_0\left[\dot{I}_1 T_{\mathrm{E}1}(x,z) + \dot{I}_2 T_{\mathrm{E}2}(x,z)\right]}{\dot{I}_1 T_{1z}(x,z) + \dot{I}_2 T_{2z}(x,z)} \tag{24}$$

One brings Equations (13) and (20) into Equation (23), and we obtain

$$Z_z(x,z) = -\frac{\mathrm{j}\omega\mu_0\left[\dot{I}_1 T_{\mathrm{E}1}(x,z) + \dot{I}_2 T_{\mathrm{E}2}(x,z)\right]}{\dot{I}_1 T_{1x}(x,z) + \dot{I}_2 T_{2x}(x,z)} \tag{25}$$

Equations (24) and (25) give a comprehensive view on the spatial impedance; however, it is hard to directly use Equations (24) and (25) to analyze the distribution and direction characteristic because $Z_x(x,z)$ and $Z_z(x,z)$ are in a format of the complex. Therefore, like the lumped parameter, the spatial impedance can also be decomposed into resistance and reactance components.

$$Z_x(x,z) = R_x(x,z) + jX_x(x,z) \tag{26}$$

$$Z_z(x,z) = R_z(x,z) + jX_z(x,z) \tag{27}$$

Then two vectors can be composed as follows:

$$R(x,z) = R_x(x,z)e_x + R_x(x,z)e_z \tag{28}$$

$$X(x,z) = X_x(x,z)e_x + X_x(x,z)e_z \tag{29}$$

The above two equations mean that the spatial resistance and spatial reactance are space vectors. At an arbitrary point in the WPT space, the resistance and reactance not only possess magnitudes, but also possess directions.

Based on Equations (24) to (29), the distribution and direction characteristics of the spatial impedance vector and the reason and factor influence of the spatial impedance vector will be analyzed in the following sections.

3. R AND X DISTRIBUTIONS AND DIRECTIONS

3.1. R and X Distributions and Directions in a Single Turn Coil Situation

The resistance distribution and reactance distribution are calculated by the following equations and are shown in Figures 2(a) and (b).

$$R(x,z) = \sqrt{R_x^2(x,z) + R_z^2(x,z)} \tag{30}$$

$$X(x,z) = \sqrt{X_x^2(x,z) + X_z^2(x,z)} \tag{31}$$

To make a comparison between the single turn coil and the WPT system, a single turn coil situation is firstly analyzed. The single turn coil is located on the xoy plane ($z = 0\,\mathrm{m}$), and the radius is 0.1 m. The cross-sections of the single turn coil are depicted in Figure 2(a).

In Figure 2(a), the red points stand for the cross-sections of the single turn coil on the xoz plane. The whole resistance equals zero, and there is no vector appearing. In Figure 2(b), the magnitude is less than the magnitude of spatial impedance in the far field and in free space. This result is in accordance with that illustration in [30]. Figure 2(b) also shows the arrows which stand for the directions on

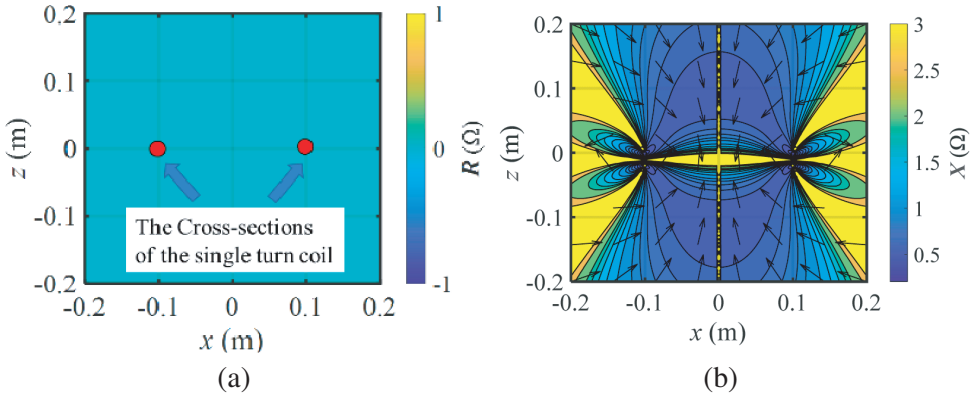

Figure 2. (a) Resistance distribution and (b) the reactance distribution.

different points on the xoz plane. The arrows have a vortex state around the cross-sections of the single turn coil. Those phenomena imply that in the near field, one coil system without any coupling state does not transmit energy to the near space. Hence there is no resistance distribution but only reactance distribution. This near space can also be regarded as the inductance region.

3.2. Typical Working Condition of a Real WPT System

A two coil WPT system is structured, shown in Figure 3(a). The WPT system comprises the source part, coil system, and load. The source includes a function signal generator, a DC source, and an amplifier. The coil system is constituted by two 0.2 m radius and 8 turn coils. The coil's parameters are measured by using the LCR Meter, and the parameters of the coil is shown in Table 1. A 10 Ω noninductive power resistance under To220 package is used as the load.

A typical working condition is tuned. We define the typical working condition of a WPT system as that the current magnitude ratio k equals 1, and the current phase difference $\Delta\phi$ equals -90 degrees.

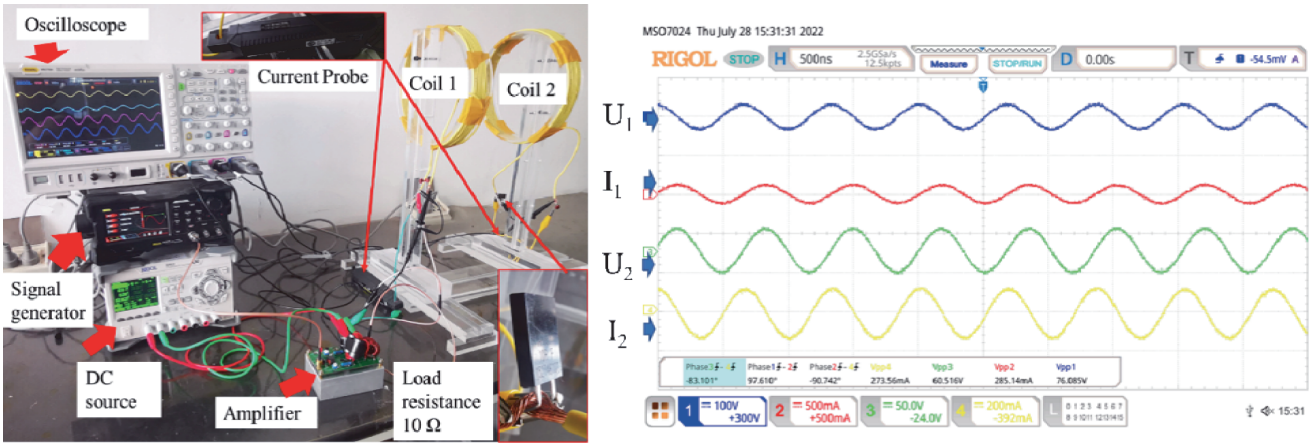

Figure 3. (a) The experimental WPT system. (b) The voltage and current waves of coil 1 and coil 2.

Table 1. Parameters of the coils.

Parameters	Radius	Turns	Inductance	Serial parasitic resistance
Values	0.2 m	8	24.06 μH	0.77 Ω

The voltage and current waves of coil 1 and coil 2 are measured and shown in Figure 3(b) under this working condition. The voltage and current phase differences (Power factor angle) are also measured. The currents are measured by using two RIGOL current probes PCA1030. U_1 and U_2 which stand for the voltages of coil 1 and coil 2, respectively. I_1 and I_2 are the currents in coil 1 and coil 2, respectively.

The current phase difference $\Delta\phi$ is equal to $-91°$, and I_1 and I_2 are equal. This result proves the existence of the defined typical working condition.

3.3. R and X Distributions and Directions in a WPT System on the Typical Working Condition

The typical working condition of a WPT system is that the current magnitude ratio k equals 1, and the current phase difference $\Delta\phi$ equals -90 degrees. This working condition can be tuned as shown in Table 2. For simplification and theoretical use, the currents of both coils are set to 1 A, and the frequency is set to 1 MHz.

Table 2. System state.

Parameters	f	U_1	I_1	φ_1	U_2	I_2	φ_2	$\Delta\phi$	Transmit power	Received power	Power loss	Efficiency
Values	1.414 MHz	38.4 V	0.14 A	83°	30.26 V	0.14 A	−83°	−91°	0.33 W	0.25 W	0.08 W	76%

Under the typical working condition, the power is transferred from coil 1 (the lower position coil) to coil 2 (the upper position coil), shown in Figure 1. The following figures will only consider the distributions or directions on the xoz plane, and four cross-sections of the coils remain, shown in Figure 1(b). The distribution and direction of the resistance $R(x, z)$ and the distribution and direction of the reactance $X(x, z)$ can be calculated by Equations (28) and (29). The results are depicted in Figure 4.

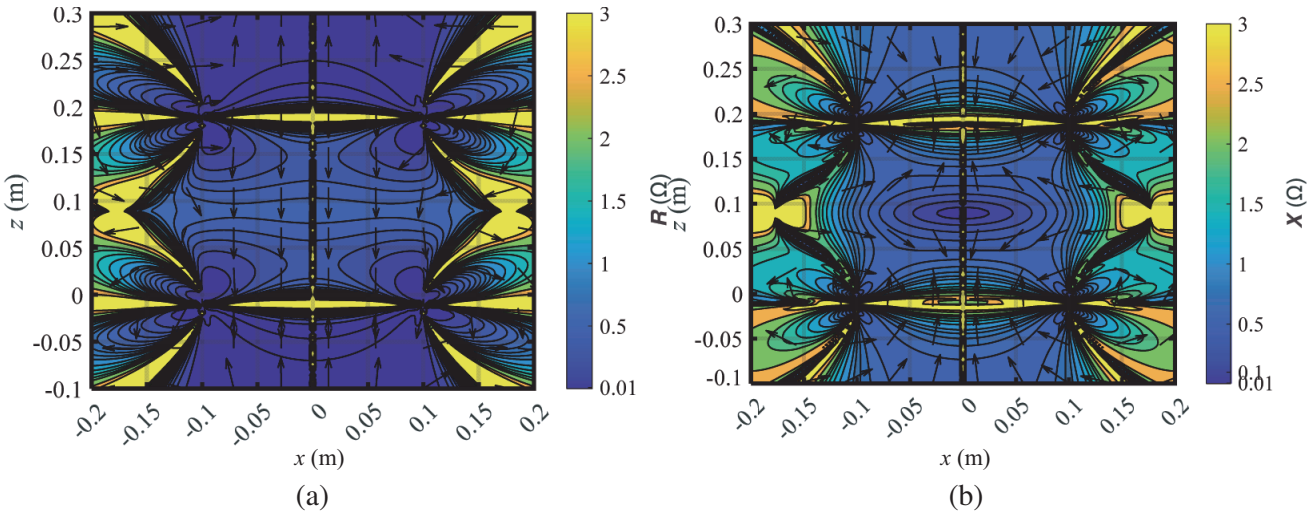

Figure 4. (a) Spatial resistance distribution and direction and (b) the spatial reactance distribution and direction of a two coils WPT system on the typical working condition.

Figure 4 shows the distribution and direction of the resistance and the reactance of a two-coil WPT system. The distribution and direction are much more complex than that in the single turn coil situation. Compared with the resistance distribution shown in Figure 2(a), the magnitude in Figure 4(a) is not equal to zero, which indicates that there is power transferring in this two-coil WPT system.

More importantly, in the region $z = -0.1\,\text{m}$ to $z = 0.1\,\text{m}$ and $x = 0\,\text{m}$ to $x = 0.2\,\text{m}$, a resistance tunnel appears. Firstly, the magnitude of this tunnel region is lower than that in other areas which are around the tunnel region. The main value of this region is $0.5\,\Omega$ under the typical working condition. Secondly, the directions of the points in the tunnel region have a unified direction which is from coil 2 to coil 1. This direction is opposite to the direction of power transferring which transfers power from coil 1 to coil 2. This result means that the resistance direction possesses a clear physical meaning, which indicates the opposite direction of the power flow. The external form of the tunnel is like a cylinder under the typical working condition of a WPT system.

Figure 4(b) shows the reactance distribution and direction. The arrows also possess a vortex state around the four cross-sections of the coils, which is similar to the state shown in Figure 2(b).

3.4. Reasons for Directions of the Resistance Tunnel

To discover why the resistance component possesses a tunnel phenomenon, the distributions of $R_x(x, z)$ and $R_z(x, z)$ can be used to analyze $R(x, z)$ because $R(x, z)$ is composed by $R_x(x, z)$ and $R_z(x, z)$, expressed in Equation (28).

Figure 5 shows the distributions of $R_x(x, z)$ and $|R_x(x, z)|$. The distribution of $R_x(x, z)$ is used to analyze the positive and negative values of $R_x(x, z)$, and the distribution of $|R_x(x, z)|$ is used to analyze the absolute value of $R_x(x, z)$.

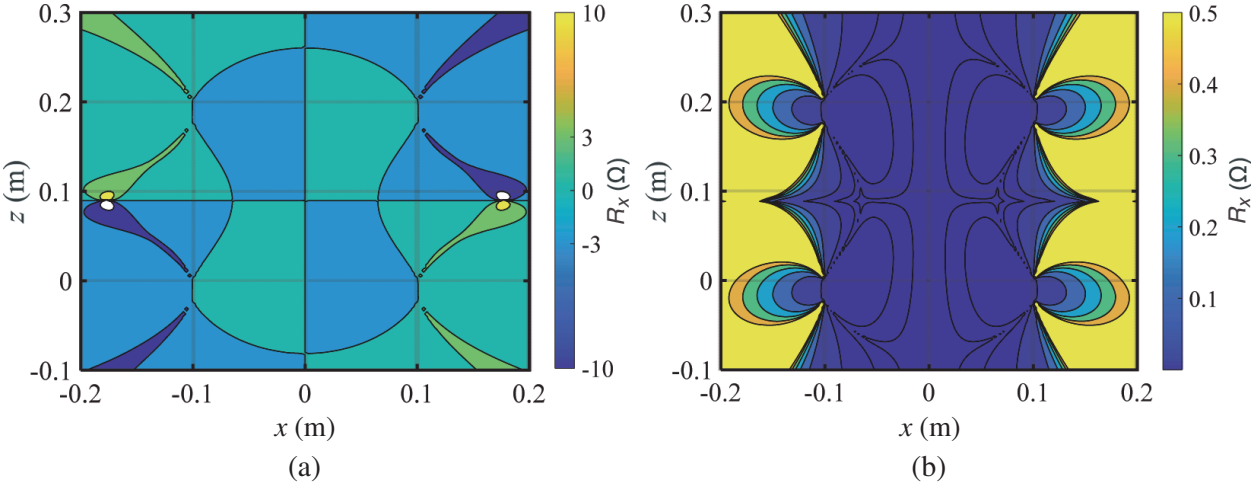

Figure 5. (a) $R_x(x, z)$ distributions with range of -10 to $10\,\Omega$. (b) $|R_x(x, z)|$ distribution with range of 0.0001 to $0.5\,\Omega$.

According to Figure 4(a), the middle region from $z = -0.1\,\text{m}$ to $z = 0.1\,\text{m}$ and $x = -0.05\,\text{m}$ to $x = 0.25\,\text{m}$ is the resistance tunnel region. Figure 5(a) shows that $R_x(x, z)$ has positive and negative values in the tunnel region. We choose values $-10\,\Omega$, $-3\,\Omega$, $0\,\Omega$, $3\,\Omega$, $10\,\Omega$ to obtain a better view on the tunnel region. Those distinct values do not cover all the rapid values on the value rapidly existing regions shown in Figure 4(a). Therefore, some boundaries appear, which seem discontinuous. Figure 5(b) shows that in the tunnel region, the absolute value of $R_x(x, z)$ is less than that in other regions. The maximum of tunnel region is less than $0.1\,\Omega$.

In Figure 6(a), the values of $R_z(x, z)$ in the tunnel region are negative. Only in the bottom or top regions, the values of $R_z(x, z)$ are positive. Figure 6(b) shows that in the tunnel region the absolute value of $|R_z(x, z)|$ is from 0.1 to $0.6\,\Omega$, which is higher than the absolute value of $|R_x(x, z)|$. This indicates that in the tunnel region, $R_z(x, z)$ is dominant. Because $R_z(x, z)$ is negative in the tunnel region, and it is dominant compared to $R_x(x, z)$, the composed vector $R(x, z)$ possesses a downward direction in Figure 4(a). This result shows the reason for the direction of the resistance tunnel.

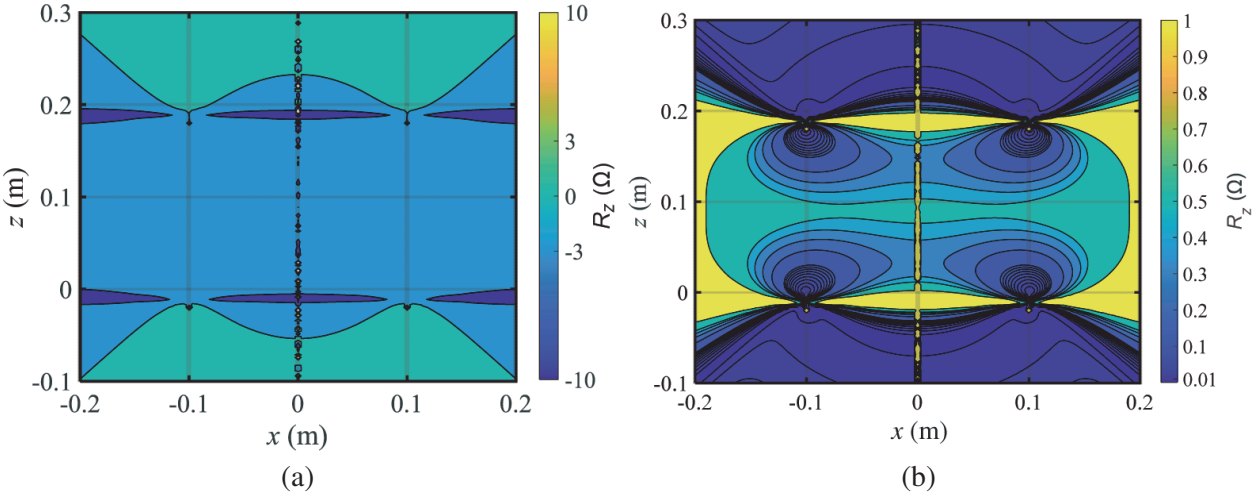

Figure 6. (a) $R_z(x, z)$ distributions with range of -10 to $10\,\Omega$. (b) $|R_z(x, z)|$ distribution with range of 0.01 to $1\,\Omega$.

3.5. Reasons for Magnitude of the Resistance Tunnel

To depict the tunnel more directly, curves on different horizontal lines have been plotted and shown in Figure 7. The vertical axis is R, and the horizontal axis is x points. The red line is the line on $z = 0.25\,\text{m}$ of the xoz plane shown in Figure 1(b); the blue triangle-line is the line on $z = 0.15\,\text{m}$; and the yellow circle-line is the line on $z = 0.1\,\text{m}$.

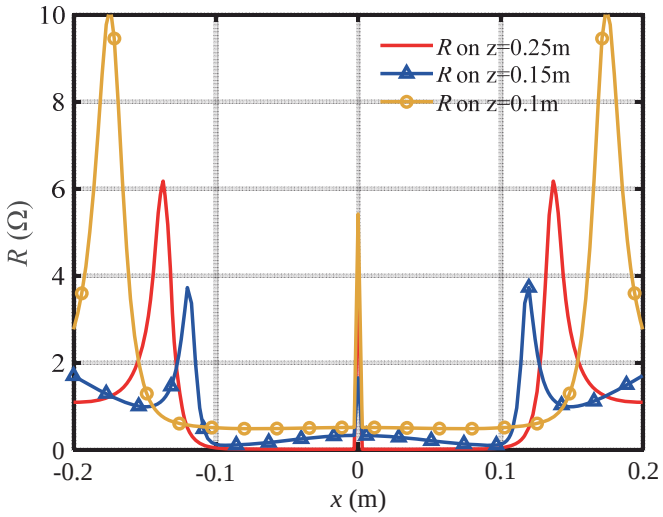

Figure 7. Resistance on different horizontal z-lines of the solenoid coil system on the typical working condition.

From Figure 7, concaves appear on all the three curves. Those concaves have two peak values in the region $x = -0.2\,\text{m}$ to $x = -0.1\,\text{m}$ and the region $x = 0.1\,\text{m}$ to $x = 0.2\,\text{m}$. Those peaks form the boundaries of the resistance tunnel, and those concaves form a power ditch to transfer the energy. This is why there is a resistance tunnel from the magnitude view.

Up to now, we have found a resistance tunnel under the typical working condition of a two-coil WPT system and analyzed the reasons for forming the resistance tunnel from the direction and magnitude views.

4. FACTORS INFLUENCE ON THE RESISTANCE TUNNEL

From Equations (24) and (25), it can be found that many factors in the WPT system will influence the spatial impedance. Those factors include the operating frequency of the WPT system, the currents carried in coils, and coils' type. Therefore, in this section factors will be taken into account to analyze their influence on the resistance tunnel. It is found that only the current phase difference determines whether the resistance tunnel exists.

4.1. Influence of the Frequency

In the lumped parameter system, the frequency does not influence the resistance but only influences the reactance. However, for the spatial impedance, according to Equations (24) and (25), the frequency will influence both the resistance and reactance. There is a linear relation between the frequency and spatial impedance, according to Equations (24) and (25). Therefore, the distributions of the magnitude of the resistance and reactance under different operating frequencies in a WPT system are proportional to the distributions shown in Figures 4(a) and (b), whereas the directions of the resistance and reactance keep the same in Figures 4(a) and (b). The results show that the frequency only influences the magnitude of the spatial impedance, but does not influence the directions of the spatial impedance.

4.2. Influence of the Currents Phase Difference

The influence of the current phase difference will be analyzed in this part. The current phase difference $\Delta\phi$ varying from 0 degrees to -180 degrees is considered, and the other factors are kept the same as the typical condition in Section 3. The negative current phase difference indicates that the transferred power is from coil 1 to coil 2. The results of the spatial resistance on $\Delta\phi$=0°, $\Delta\phi$=$-45°$, and $\Delta\phi$=$-135°$ are depicted in Figures 8(a), (b), and (c), respectively. The result of $\Delta\phi = -180°$ is the same as that of $\Delta\phi = 0°$, and the result of $\Delta\phi = -90°$ is analyzed in Figure 4.

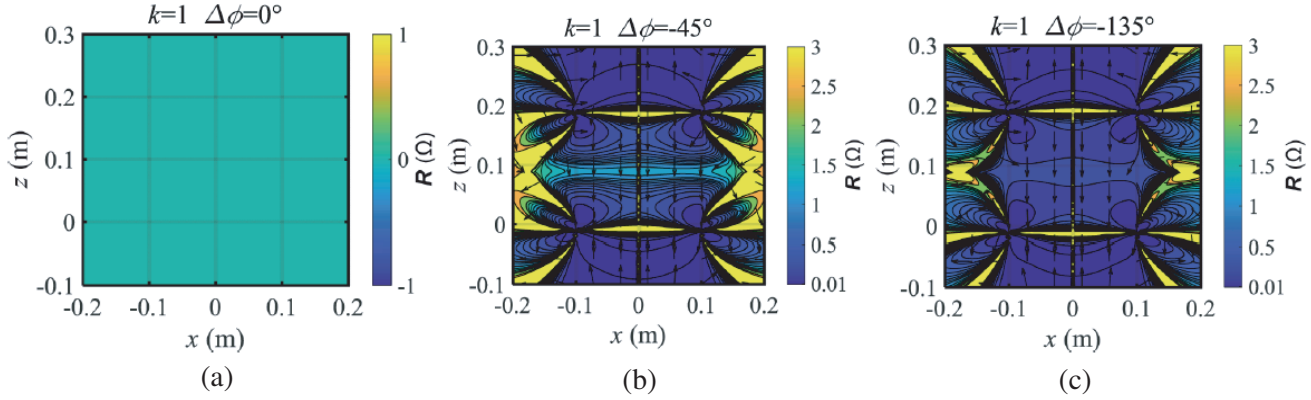

Figure 8. The resistance distributions and directions on (a) $\Delta\phi = 0°$, (b) $\Delta\phi = -45°$, (c) $\Delta\phi = -135°$.

Figure 8(a) shows the spatial resistance of the condition of $\Delta\phi = 0°$. There are no vector arrows, and the magnitude at arbitrary point is equal to zero. The result is the same as that in the single turn coil's situation shown in Figure 2(a). This is because under the condition of $\Delta\phi = 0°$ or $-180°$, there is no current phase difference, hence the two coils coupling system is decoupled. The resistance distribution of the two coils WPT system is simply superposed by two individual single coils. This result also indicates that there is no power flow on the conditions of $\Delta\phi = 0°$ or $\Delta\phi = -180°$.

On the other hand, if $\Delta\phi \neq 0°$ or $-180°$, the vector arrows of the resistance vector exist, and the magnetic filed of the resistance vector does not equal to zero. This shows that a condition of the WPT transferring the energy is of $\Delta\phi \neq 0°$ or $-180°$. On the condition $\Delta\phi \neq 0°$ or $-180°$, the resistance vectors form a tunnel which is like the tunnel in the typical condition, and the vector arrows are from coil 2 to coil 1 in the middle region between coil 1 and coil 2.

4.3. Influence of the Current Magnitude Ratio

This part will discuss the influence of the current magnitude ratio k, which varies from $k = 100$ to $k = 0.01$. Figure 9 shows the resistance magnitude distributions and vector directions on four different k values. The condition $k = 100$ means that the magnitude of the current in coil 2 is 100 times of that in coil 1.

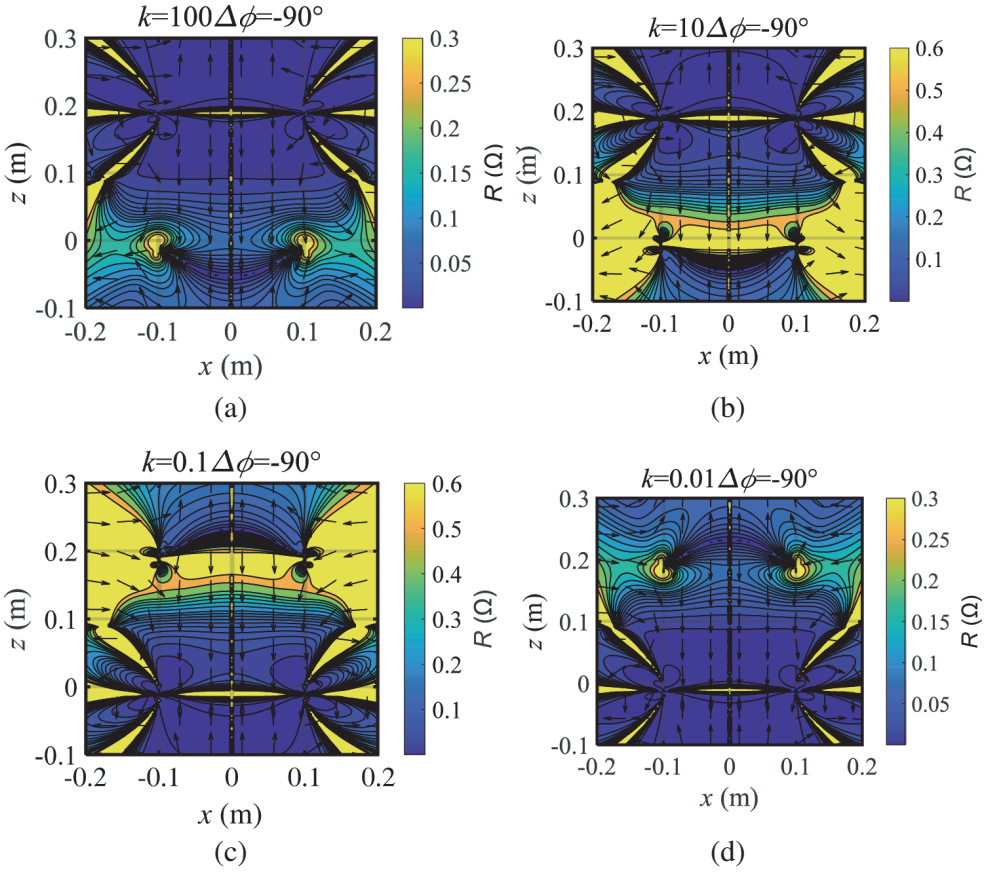

Figure 9. The resistance distributions and directions on (a) $k = 100$, (b) $k = 10$, (c) $k = 0.1$, (d) $k = 0.01$.

From Figure 9, it can be inferred that the current magnitude ratio or the relative magnitude of the two currents will influence the magnitude of the resistance distributions. The current magnitude ratio will also influence the vector arrows of the resistance. However, this influence only changes the arrows' directions on the region $x = -0.2\,\text{m}$ to $x = -0.1\,\text{m}$ and the region $x = 0.1\,\text{m}$ to $x = 0.2\,\text{m}$, which is not in the resistance tunnel. There still exists a resistance tunnel in the middle region between two coils from $x = -0.1\,\text{m}$ to $x = 0.1\,\text{m}$.

With the consideration that the conditions $k = 100$ to $k = 0.01$ almost cover all situations which may appear in the real working condition of the WPT system, one can make a conclusion that no matter what current magnitude in a WPT system, a resistance tunnel must appear.

To illustrate the resistance tunnel more directly from the magnitude view, several curves which are on different horizontal z lines under the condition of $k = 100$ is shown in Figure 10. The red line is the line on $z = 0.15\,\text{m}$; the blue triangle-line is the line on $z = 0.1\,\text{m}$; and the yellow circle-line is the line on $z = 0.05\,\text{m}$. All the three curves appear concave from $x = -0.1$ to $x = 0.1$, which is the main part of the resistance tunnel. Compared to the curves shown in Figure 7, the positions and magnitude of the peaks of the curves are changed in Figure 10, but the concave phenomenon still exists.

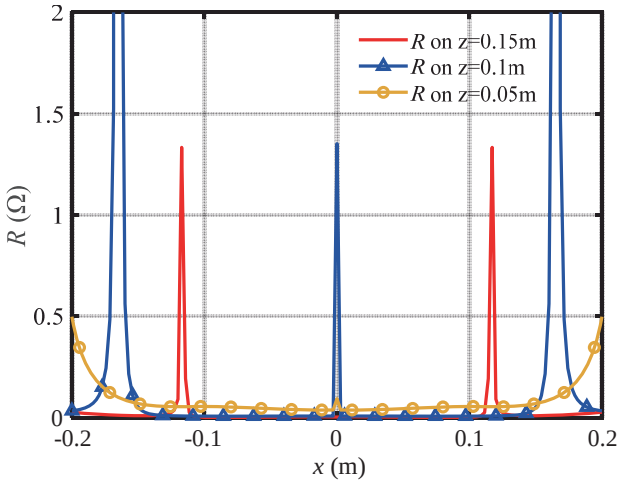

Figure 10. The resistance magnitude R_{mag} on different z lines on the condition $k = 100$.

4.4. Influence of the Coil Type

The last factor that will influence the spatial impedance is the coil type. In the former analyses, we only considered the solenoid coils with 8 turns. In this part, we will use 8 turns spiral coils which are also commonly used in the design of a WPT system. The spatial impedance includes the resistance and reactance distributions, and directions are shown in Figure 11. Compared to the resistance and reactance shown in Figure 4, the resistance and reactance of the spiral coil system are similar to that in the solenoid coil system. There are only small differences between the two situations, but the resistance tunnel, shown in Figure 11(a), still exists.

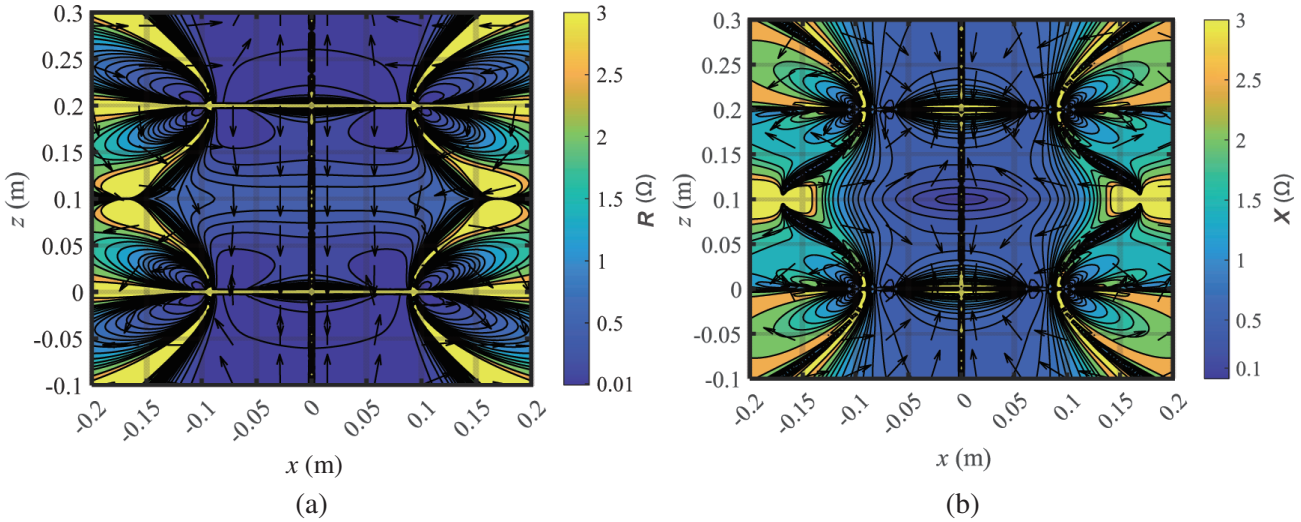

Figure 11. (a) The spatial resistance distribution and direction and (b) the spatial reactance distribution and direction of a two spiral coils WPT system on the typical working condition.

To give a more direct view of the resistance tunnel, three curves on different horizontal z-lines of the resistance distribution shown in Figure 11(a) are also presented in Figure 12. In Figure 12, the red line is the line on $z = 0.25$ m; the blue triangle-line is the line on $z = 0.15$ m; and the yellow circle-line is the line on $z = 0.1$ m. All the three curves possess concave phenomenon, which indicates that the curves will form a tunnel in 3-D situation. This also implies that no matter what coil type is, a resistance tunnel exists in the WPT space.

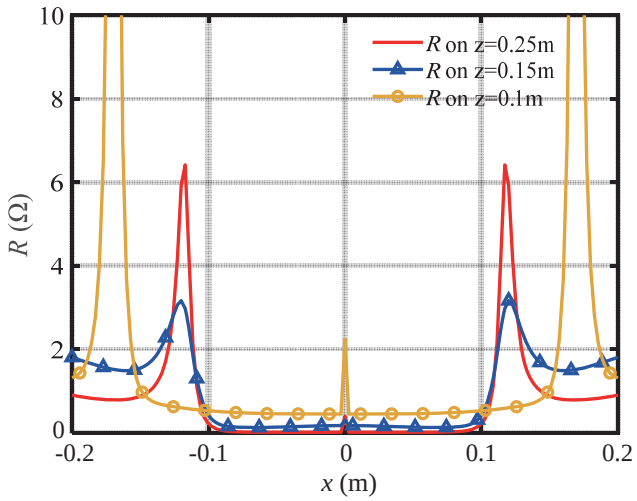

Figure 12. The resistance on different horizontal z-lines of the spiral coil system on the typical working condition.

5. VERIFICATION

To verify the existence and analysis of the spatial resistance tunnel, an electromagnetic simulation is presented in this Section. The simulation is conducted via ANSYS Electromagnetic Suit, and the governing equations are as follows:

$$\begin{cases} \nabla \times \dot{H}(x,y,z) = \dot{J}_s(x,y,z) \\ \nabla \times \dot{E}(x,y,z) = -j\omega \dot{B}(x,y,z) \\ \nabla \cdot \dot{H}(x,y,z) = 0 \end{cases} \tag{32}$$

The considered situation of the electromagnetic field is magnetoquasistatic field, and the space displacement current is also considered. The WPT system has two 8 turn 0.1 m radius solenoid coils separated by 0.2 m along the z-axis. The figure of the coils is shown in Figure 13(a). The spatial distribution and distribution of the resistance vector are also presented in Figures 13(a) and (b). In Figure 13(a), the arrows between two coils are downward, which indicate a resistance tunnel the same as that in Figure 4(a). In Figure 13(b), the resistance magnitude distribution is similar to that

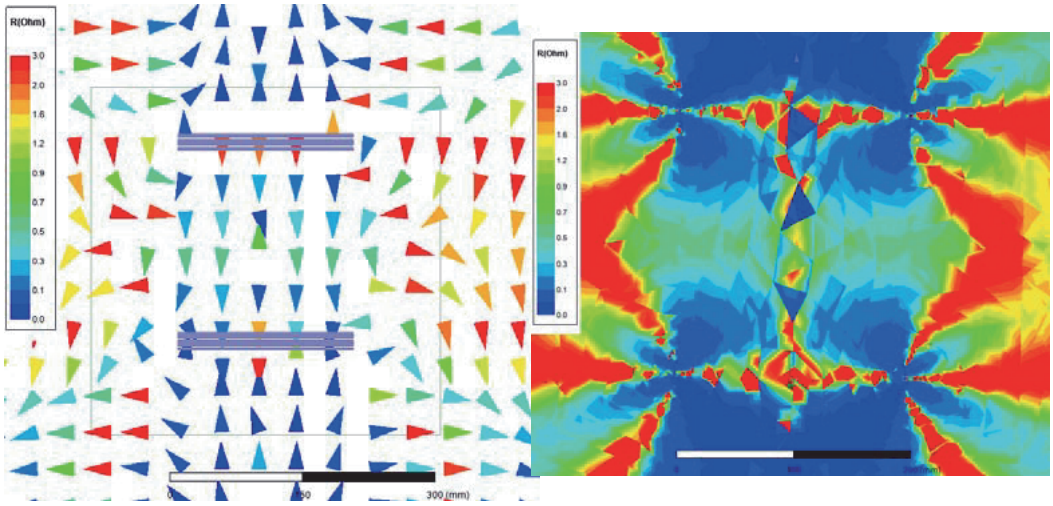

(a) (b)

Figure 13. The resistance vector (a) direction and (b) distribution of the WPT system via simulation.

in Figure 4(a). This result shows that the former analyses are correct. In Figure 13(b), there are many fragments-like parts, which are different from Figure 4(a). This is because the simulation uses FEM, which needs to mesh the space, resulting in some discontinuous values on the boundaries of the meshed units. Hence, a smooth function is used in the plotting of the calculated field, which makes the magnetic or electric fields continuous. However, the postprocessing fields, including the resistance and reactance distributions, cannot be continuous even when one adopts the smooth function. But the locally discontinuous boundaries do not influence the whole tendency of the magnitude of the resistance distribution, which is similar to the distribution shown in Figure 4(a).

To present a more direct view on the comparison of the theoretical calculation and the simulation, two resistance magnitude curves on the horizontal z-line on $z = 0.1$ are presented in Figure 14. The whole tendencies of the two curves are the same, and both the curves appear concave. On the points $x = -0.18$, 0, and 0.18, same differences appear. This is because in those regions, the value of the resistance changes rapidly, and the value rapidly changed region is small. The FEM simulation cannot always obtain an exact result on those value rapidly changing regions. Hence, the simulation result and theoretical calculation show difference in those regions. However, we concern the bottom region from -0.1 to 0.1, which is the resistance tunnel region. The peak value appearing region does not influence the comparison to the tunnel region. This result proofs the correctness of the theoretical calculation.

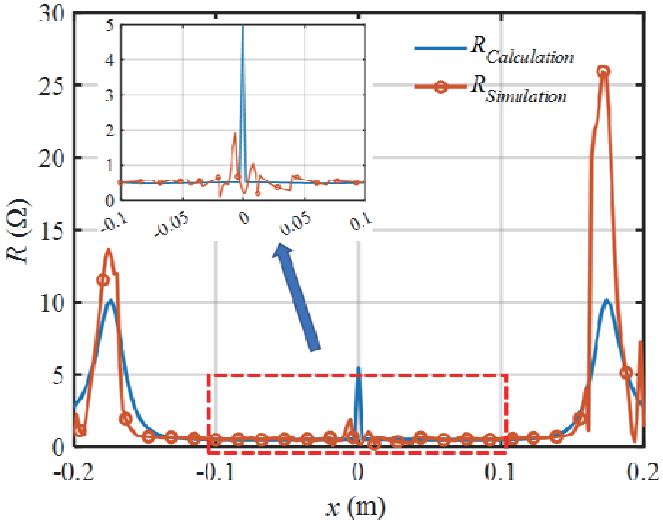

Figure 14. The comparison of the resistance curves on $z = 0.1$ by theoretical calculation and simulation.

Above all, the simulation conducted by FEM proofs the correctness of the theoretical analysis and also proofs the existence of the resistance tunnel.

6. CONCLUSION

This paper analyzes the spatial impedance of the power transferring space of a WPT system and discovers that a resistance tunnel exists, which is the main region of the power transferring space. The spatial impedance is a vector in space and contains a resistance part and a reactance part. The resistance part and reactance part are also extended to a form of vector. By using the $R(x, z)$ vector definition, the resistance tunnel of the $R(x, z)$ vector is discovered.

Four factors are analyzed, and it is found that only the current phase difference determines the existence of the resistance tunnel. The frequency, current magnitude ratio, and coil type only influence the magnitude and direction of the resistance.

Since WPT system is one of the typical coupling systems in the near field, one can infer that the resistance tunnel not only exists in the WPT system, but also exists in other coupling coil systems in the near field.

ACKNOWLEDGMENT

This work was supported financially by the National Natural Science Foundation of China (Grant No. 52007159)and the Natural Science Foundation of Southwest University of Science and Technology (Grant No. 20zx7116).

REFERENCES

1. Khan, N., H. Matsumoto, and O. Trescases, "Wireless electric vehicle charger with electromagnetic coil-based position correction using impedance and resonant frequency detection," *IEEE Trans. Power Electr.*, Vol. 35, No. 8, 7873–7883, 2020.
2. Kadem, K., F. Benyoubi, M. Bensetti, Y. L. Bihan, E. Labour'e, and M. Debbou, "An efficient method for dimensioning magnetic shielding for an induction electric vehicle charging system," *Progress In Electromagnetics Research*, Vol. 170, 153–167, 2021.
3. Kim, Y. G. and S. Nam, "Determination of the impedance parameters of antennas and the maximum power transfer efficiency of wireless power transfer," *IEEE Trans. Antenn. Propag.*, Vol. 67, No. 8, 5132–5144. 2019.
4. Arabsalmanabadi, B., H. Arab, V. H. G. Amador, S. Dufour, and K. Al-Haddad, "A three-dimensional discontinuous Galerkin time-domain finite element method for electromagnetic modeling of wireless power transfer coils," *IEEE Open Journal of the Industrial Electronics Society*, Vol. 2, 360–371, 2021.
5. Zhang, K., L. Du, Z. Zhu, B. Song, and D. Xu, "A normalization method of delimiting the electromagnetic hazard region of a wireless power transfer system," *IEEE Trans. Electromagn. C.*, Vol. 60, No. 4, 829–839, 2018.
6. Chabalko, M., J. Besnoff, M. Laifenfeld, and D. S. Ricketts, "Resonantly coupled wireless power transfer for non-stationary loads with application in automotive environments," *IEEE Trans. Ind. Electron.*, Vol. 64, No. 1, 91–103, 2017.
7. Li, W., Q. Wang, J. Kang, and Y. Wang, "Energy distribution characteristics of magnetically coupled resonant wireless power transfer systems considering four basic reactive power compensations," *Progress In Electromagnetics Research M*, Vol. 86, 1–16, 2019.
8. Kang, J., Q. Wang, Y. Wang, and W. Li, "Polarization characteristic of the magnetic field in wireless power transfer systems," *IEEE Trans. Antenn. Propag.*, Vol. 67, No. 11, 7114–7120, 2019.
9. Chu, S. Y., X. Zan, and A. Avestruz, "Electromagnetic model-based foreign object detection for wireless power transfer," *IEEE Trans. Power Electr.*, Vol. 37, No. 1, 100–113, 2022.
10. Shah, I. A. and H. Yoo, "Assessing human exposure with medical implants to electromagnetic fields from a wireless power transmission system in an electric vehicle," *IEEE Trans. Electromagn. C.*, Vol. 62, No. 2, 338–345, 2020.
11. Park, S., "Evaluation of electromagnetic exposure during 85 kHz wireless power transfer for electric vehicles," *IEEE Trans. Magn.*, Vol. 54, No. 1, 1–8, 2018.
12. Lu, C., C. Rong, X. Huang, Z. Hu, T. Xiong, S. Wang, et al., "Investigation of negative and near-zero permeability metamaterials for increased efficiency and reduced electromagnetic field leakage in a wireless power transfer system," *IEEE Trans. Electromagn. C.*, Vol. 61, No. 5, 1438–1446, 2019.
13. Lee, S., D. H. Kim, Y. Cho, H. Kim, C. Song, S. Jeong, et al., "Low leakage electromagnetic field level and high efficiency using a novel hybrid loop-array design for wireless high power transfer system," *IEEE Trans. Ind. Electron.*, Vol. 66, No. 6, 4356–4367, 2019.
14. Bocan, K. N., M. H. Mickle, and E. Sejdic, "Multi-disciplinary challenges in tissue modeling for wireless electromagnetic powering: A review," *IEEE Sens. J.*, Vol. 17, No. 20, 6498–6509, 2017.
15. Wenngren, S., A. Clements, and T. Johnson, "Capacitively coupled resonator models for investigating spatial impedance variation in WPT systems," *2018 IEEE Wireless Power Transfer Conference (WPTC)*, 1–4, 2018.

16. Karami, H. and K. Sheshyekani, "Harmonic impedance of grounding electrodes buried in a horizontally stratified multilayer ground: A full-wave approach," *IEEE Trans. Electromagn. C.*, Vol. 60, No. 4, 899–906, 2018.
17. Chen, Z., K. Solbach, D. Erni, and A. Rennings, "Electromagnetic field analysis of a dipole coil element with surface impedance characterized shielding plate for 7-T MRI," *IEEE Trans. Microw. Theory*, Vol. 64, No. 3, 972–981, 2016.
18. Salarieh, B., H. M. J. De Silva, A. M. Gole, A. Ametani, and B. Kordi, "An electromagnetic model for the calculation of tower surge impedance based on thin wire approximation," *IEEE Trans. Power Deliver.*, Vol. 36, No. 2, 1173–1182, 2021.
19. Jameson, N. J., M. H. Azarian, and M. Pecht, "Impedance-based condition monitoring for insulation systems used in low-voltage electromagnetic coils," *IEEE Trans. Ind. Electron.*, Vol. 64, No. 5, 3748–3757, 2017.
20. Thiel, D. V. and R. Mittra, "Self-consistent impedance method for the solution of electromagnetic problems," *2000 Asia-Pacific Microwave Conference, Proceedings (Cat. No. 00TH8522)*, 281–285, 2000.
21. Pao, H. and J. R. Wait, "Electromagnetic induction and surface impedance in a half-space from an overhead moving current system," *IEEE Trans. Antenn. Propag.*, Vol. 48, No. 9, 1301–1305, 2000.
22. Tkachova, T. I., V. I. Shcherbinin, and V. I. Tkachenko, "Validity of surface impedance model for electromagnetic analysis of a corrugated gyrotron cavity," *2018 IEEE 17th International Conference on Mathematical Methods in Electromagnetic Theory (MMET)*, 238–241, 2018.
23. Chialina, S., M. Cicuttin, L. Codecasa, R. Specogna, and F. Trevisan, "Plane wave excitation for frequency domain electromagnetic problems by means of impedance boundary condition," *IEEE Trans. Magn.*, Vol. 51, No. 3, 1–4, 2015.
24. Hanson, G. W., "A common electromagnetic framework for carbon nanotubes and solid nanowires — Spatially dispersive conductivity, generalized Ohm's law, distributed impedance, and transmission line model," *IEEE Trans. Microw. Theory*, Vol. 59, No. 1, 9–20, 2011.
25. Chen, M., C. Wang, X. Cheng, C. Gong, W. Song, X. Yuan, et al., "Experimental demonstration of invisible electromagnetic impedance matching cylindrical transformation optics cloak shell," *J. Optics — UK*, Vol. 20, No. 4, 45608, 2018.
26. Yu, D., S. He, X. Chen, G. Zhu, and H. Yin, "Simulation of electromagnetic scattering for 3-D impedance surface using MoM-PO method," *IEEE Trans. Antenn. Propag.*, Vol. 60, No. 8, 3988–3991, 2012.
27. Upton, M. E. G. and A. C. Marvin, "The fields due to a small loaded loop in free space," *IEEE Trans. Electromagn. C.*, Vol. 36, No. 1, 7–13, 1994.
28. Amin, S., B. Ahmed, M. Amin, M. I. Abbasi, A. Elahi, and U. Aftab, "Establishment of boundaries for near-field, fresnel and Fraunhofer-field regions," *2017 IEEE Asia Pacific Microwave Conference (APMC)*, 57–60, 2017.
29. Brunett, J. D., V. V. Liepa, and D. L. Sengupta, "Extrapolating near-field emissions of low-frequency loop transmitters," *IEEE Trans. Electromagn. C.*, Vol. 47, No. 3, 635–641, 2005.
30. Orfanidis, S. J., *Electromagnetic Waves & Antennas*, online: www.ece.rutgers.edu/∼orfanidi/ewa, 2002.
31. Kang, J., Q. Wang, Y. Wang, and W. Li, "Optimization of the magnetic field computation in wireless power transfer system by two-dimensional feature selective validation and maximum value filtered method," *IEEE Trans. Electromagn. C.*, Vol. 61, No. 4, 1061–1071, 2019.
32. McLean, J. and R. Sutton, "The quasi-static near electric field of an inductive power transfer system," *2013 IEEE Symposium on Product Compliance Engineering (ISPCE)*, 1–6, 2013.
33. Papazov, S. P. and I. K. Daskalov, "Effect of contour shape of nervous system electromagnetic stimulation coils on the induced electrical field distribution," *Biomed. Eng. Online*, Vol. 1, No. 1, 1, 2002.